1   **Replacement of microglia by brain-engrafted macrophages provide long term protection**

2   **against brain irradiation and concussive injury**

3   Xi Feng[1,2], Elma S. Frias[1,2], Maria S. Paladini[1,2], David Chen[1,2,3], Zoe Boosalis[1,2],McKenna

4   Becker[1,2], Sonali Gupta[1,2], Sharon Liu[3], Nalin Gupta[3,6,7] and Susanna Rosi[1,2,3,4,5*]

5

6

7

8   [1] Brain and Spinal Injury Center

9   [2] Department of Physical Therapy and Rehabilitation Science

10   [3] Department of Neurological Surgery

11   [4] Weill Institute for Neuroscience

12   [5] Kavli Institute of Fundamental Neuroscience

13   [6] Brain Tumor Research Center

14   [7] Department of Pediatrics

15   University of California San Francisco

16

17   * Corresponding Author

18   Susanna Rosi Ph.D.: Susanna.Rosi@ucsf.edu

19   1001 Potrero Ave, Building 1, Room 101, Zuckerberg San Francisco General Hospital
20   Department of Physical Therapy and Rehabilitation Science, University of California, San
21   Francisco, San Francisco, CA 94110

22

25

Abstract

Brain resident microglia have a distinct origin compared to macrophages in other organs. Under physiological conditions, microglia are maintained by self-renewal from the local pool, independent of hematopoietic progenitors. Pharmacological depletion of microglia during therapeutic whole-brain irradiation prevents synaptic loss and long-term recognition memory deficits but the mechanisms behind these protective effects are unknown. Here we demonstrate that after a combination of therapeutic whole-brain irradiation and microglia depletion, macrophages originating from circulating monocytes engraft into the brain and replace the microglia pool. Comparisons of transcriptomes reveal that brain-engrafted macrophages have an intermediate phenotype that resembles both monocytes and embryonic microglia. Brain-engrafted macrophages display reduced phagocytic activity for synaptic compartments compared to microglia from normal brains in response to a secondary concussive brain injury. In addition to sparing mice from brain radiotherapy-induced long-term cognitive deficits, replacement of microglia by brain-engrafted macrophages can prevent concussive injury-induced memory loss. These results demonstrate the long-term functional role of brain-engrafted macrophages as a possible therapeutic tool against radiation-induced cognitive deficits.

43

Introduction

45   Brain resident microglia are the innate immune cells of the central nervous system (CNS).

46 Arisen from the yolk sac during embryonic development, microglia actively survey the

47 environment to maintain normal brain functions [1,2]. Under physiological conditions, microglia are

48 maintained solely by self-renewal from the local pool [3]. Following brain injury and other

49 pathological conditions, microglia become activated and play a central role in the clearance of

50 cellular debris, but if not controlled this process can result in aberrant synaptic engulfment [4-7].

51 Temporary depletion of microglia can be achieved by using pharmacologic inhibitors of the

52 colony-stimulating factor 1 receptor (CSF-1R) [8]. In the normal brain, treatment with CSF-1R

53 inhibitors (CSF-1Ri) can deplete up to 99% of microglia without causing detectable changes to

54 cognitive functions [8,9]. Full repopulation occurs within 14 days of inhibitor withdrawal and the

55 repopulated microglia are morphologically and functionally identical to the microglia in naïve

56 brains [9]. Microglia depletion and repopulation by local progenitors has been shown to be beneficial

57 for disease- ,injury- , and age-associated neuropathological and behavioral conditions[10-15].

58 However, the mechanisms for these protective effects are unknown.

59   Whole-brain radiotherapy (WBRT), delivered in multiple fractions, is routinely used to treat

60 patients with brain tumors. It is estimated that more than 200,000 patients receive WBRT yearly

61 in the US alone [16]. While it is effective in improving intracranial tumor control, WBRT leads to

62 deterioration of patients' cognitive functions and quality of life [17-19]. Currently, there is no treatment

63 available to prevent or mitigate these adverse effects. Previous studies demonstrated that WBRT

64 causes deleterious effects to the CNS microenvironment by a number of mechanisms including

65 apoptosis of neural progenitor cells, disruption of the blood-brain barrier, activation of microglia

66 and accumulation of peripherally derived macrophages [20-25]. We and others have reported that

67 depletion of microglia during or shortly after brain irradiation in animal models can prevent loss of

3

68 dendritic spines in hippocampal neurons and cognitive impairments that develop at later time

69 points [12-14]. These reports suggest that microglial plays a critical role in inducing synaptic

70 abnormalities and consequently, cognitive deficits after brain irradiation. The underlying molecular

71 pathways responsible for the protective effects of repopulated microglia against radiotherapy-

72 induced neuronal alterations remain unknown.

73   In the current study, 1) we first defined signature of repopulating cells and analyzed the

74 transcriptional profile of repopulated brain macrophages from irradiated mouse brains after CSF-

75 1R inhibitor-mediated depletion. 2) We next sought to establish the origin of repopulated cells

76 coming from the peripheral monocytic lineage. 3) We identified the functionality of repopulated

77 macrophages by measuring the ability to engulf synaptic compartments compared to brain

78 resident microglia. Lastly, 4) we determined the protective properties of brain-engrafted

79 macrophages (BEMs) against a secondary concussive brain injury-induced cognitive deficits.

80 Together, these results uncover the mechanism by which brain-engrafted macrophages preserve

81 hippocampal synapses and memory functions after radiation injury and also in response to an

82 additional brain injury.

83

84 **Results**

85 *Microglia depletion and repopulation prevents long term radiation-induced memory deficits and*

86 *loss of hippocampal PSD95.*

87 Temporary microglia depletion during or shortly after exposure to brain irradiation prevents

88 cognitive deficits, suggesting microglia's key role in modifying neuronal and cognitive functions [12-

89 14]. Changes in expression levels of pro-inflammatory cytokine/chemokines have been shown to

90 correlate with cognitive performance in mice [12, 15, 20], however, the exact change in the

91 transcriptional profile of repopulated microglia after brain irradiation is unknown and is an

92 important tool to dissect the roles that repopulated microglia play in preventing of radiation-

93 induced memory deficits. We performed RNA sequencing using repopulated microglia, FACS

94 sorted from irradiated and control mouse brains after CSF-1Ri treatment, and compared with

95 transcriptomes of microglia obtained from mice without CSF-1Ri treatment (**Figure 1a,b**). A CSF-

96 1R inhibitor was used to fully deplete microglia in 8-weeks old male mice, for a duration of 21

97 days. Three fractions of therapeutic whole-brain irradiation were given to each mouse every other

98 day over five days starting from day 7 of CSF-1R inhibitor treatment. Novel Object Recognition

99 (NOR) test was used to measure recognition memory 4 weeks after the last fraction of WBRT.

100 Consistent with our previous report, fractionated WBRT resulted in impairment in recognition

101 memory, which was prevented by CSF-1R inhibitor treatment (**Figure 1a, lower panel**). One day

102 after the NOR test, mice were euthanized and whole brains were used to sort microglia

103 (CD45^{low}CD11b$^+$ population) for RNA extraction. We used samples from the five best performers

104 in non-impaired groups (control diet + sham, CSF-1R inhibitor + sham/WBTR) and the five worst

105 performers in the memory impaired group (control diet + WBRT) for RNA sequencing (**Figure 1a**).

106 We previously demonstrated that brain irradiation resulted in reduced density of dendritic spines

107 in hippocampal neurons [13]. To accurately determine the effect of WBRT in the intrinsic synaptic

108 protein levels we measured pre- and post-synaptic markers in the hippocampus by flow-

109   synaptometry [26, 27]. Fractionated hippocampal cell membranes containing synaptosomes were

110   enriched and particles between 1 – 3 μm were analyzed to measure synaptic protein levels using

111   mean fluorescent intensities by FACS (**Figure 1e**). We observed no changes in pre-synaptic

112   Synapsin-1 protein levels in the hippocampi across all groups (**Figure 1f**). However, we measured

113   a significant reduction in post-synaptic protein PSD-95 after WBRT, which was completely

114   prevented by CSF-1R inhibitor mediated microglia depletion (**Figure 1g**). These results cement

115   the role of microglia in the radiation-induced loss of post-synaptic components after WBRT.

116

117   *Microglia depletion and repopulation eliminates radiation-induced transcriptome signatures*

118   To identify biological pathways involved in radiation-induced memory deficits, we listed genes

119   differentially expressed in microglia after WBRT with and without microglia depletion and

120   repopulation for Gene Ontology Biological Process (GOBP) enrichment analysis. 204 genes were

121   found to be differentially expressed (DE genes) only in microglia isolated from irradiated brains

122   (**Figure 1b and Supplementary Table 1**). No enriched GOBP terms were found from the 87

123   WBRT down-regulated genes (Supplementary Table 1). There were 193 enriched GOBP terms

124   from the 117 WBRT up-regulated genes, the top 20 enriched GOBP terms are listed in **Figure 1c.**

125   Almost half (96) of these enriched GOBP terms were associated with increased response to cell

126   cycle regulation, radiation, DNA repair and stress; the rest enriched GOBP terms were associated

127   with increased metabolism (21), development (12), regulation of protein kinase activity (8), cellular

128   adhesion (4) and other functions (**Figure 1d, Supplementary Table** 1). Notably, regardless of

129   WBRT, the expression of these WBRT-induced DE genes did not change in cells isolated from

130   brains treated with CSF-1Ri. These results demonstrate that the transcriptomic changes in

131   microglia induced by WBRT can be completely eliminated after microglia depletion and

132   repopulation.

133

qPCR validation of the RNAseq results

135   To validate the RNAseq results, we next performed qPCR analyses using sorted microglia from

136   animals in the same cohort (**Figure 1b,** and **Supplementary Table 1**). The expression of the toll-

137   like receptor 3 (TLR3) family gene *Lgals9* was significantly increased by irradiation (WBRT +

138   Control diet versus Sham + Control diet) and was at levels comparable to the shams (Sham +

139   Control diet) when treated with CSF-1Ri despite of irradiation (**Supplementary Figure S1a**).

140   *TNFα*, another TLR3 family member which also belongs to GOBP "regulation of response to

141   reactive oxygen species (ROS)", was significantly upregulated by irradiation (WBRT + Control

142   diet versus Sham + Control diet); its expression levels are comparable between the Sham +

143   Control diet and the WBRT + CSF1Ri treated groups. However, *TNFα* remained elevated in

144   microglia from mice treated only by CSF-1Ri (Supplementary Figure S1b). Another gene from the

145   GOBP "regulation of response to ROS", *Sesn2*, was also significantly upregulated by WBRT

146   (**Supplementary Figure S1c**). *Sesn2* remained at the control sham levels in CSF-1Ri only group

147   and was significantly down-regulated in the WBRT + CSF-1Ri group. *Mdm2*, a gene that belongs

148   to GOBP "cellular response to ionizing radiation", was increased after WBRT, and significantly

149   downregulated in in CSF-1Ri treated groups (Supplementary Figure S1d). Other WBRT-induced

150   expression of radiation induced genes, *Ddias*, *Rad51, FoxM1* and *Check 1*, were all at the control

151   sham levels in repopulated microglia regardless of the exposure to WBRT (**Supplementary**

152   **Figure S1 e – h**). In conclusion, the qPCR validation confirmed that the transcriptomic changes

153   seen in our RNAseq dataset were reliable. These results suggest that CSF-1Ri mediated

154   microglia depletion during WBRT followed by repopulation eliminated radiation-induced

155   signatures in the microglia transcriptome.

156

157 *Repopulated microglia after WBRT originate from peripheral monocytes*

158 The fractalkine receptor CX3CR1 is expressed in both microglia and peripheral monocytes [28],

159 while chemokine receptor CCR2 is mainly expressed in monocytes [29]. In the Cx3cr1[GFP/+]Ccr2[RFP/+]

160 reporter mice, the different expression patterns of GFP and RFP can be used to distinguish

161 microglia (GFP+RFP-) from monocytes (GFP+RFP+) [29]. To investigate the cell-of-origin of

162 repopulated microglia in our experimental paradigm we generated bone marrow chimeras with

163 head-protected irradiation using fluorescent labeled bone marrow from Cx3cr1[GFP/+]Ccr2[RFP/+]

164 donor mice (**Figure 2a**). This allowed partial replacement of bone marrow cells without changing

165 the permeability of the blood-brain-barrier [2, 30, 31]. At 6 weeks after bone marrow transplantation

166 about two thirds of peripheral monocytes were replaced by transplanted cells with fluorescent

167 labels (**Figure 2b**). Bone marrow chimera animals were then treated with WBRT and CSF-1R

168 inhibitor following the same experimental timeline used for RNA sequencing (**Figure 2a**). Next,

169 we compared the compositions of myeloid cells in the brain after CSF-1R inhibitor-mediated

170 depletion and repopulation. Flow cytometry analyses performed 33 days after WBRT revealed

171 that microglia depletion and repopulation alone (Sham + CSF-1Ri) only resulted in limited

172 accumulation of transplanted cells in the brain (**Figure 2c, BMT only**). However, in mice that

173 received WBRT and CSF-1Ri, two thirds of the microglia were replaced by Cx3cr1-GFP labeled

174 cells (**Figure 2c, BMT +fWBI**). These results suggest that microglia depletion during WBRT

175 resulted in significant contribution of the CNS microglia pool by peripheral monocyte-derived

176 BEMs.

177

178 *Brain-engrafted macrophages retain monocyte signatures*

179 We next assessed the transcriptomic signature of the BEMs after microglia depletion and WBRT

180 by comparing our RNAseq dataset with a previous report by Lavin and Winter *et al* [32]. To minimize

181   false discovery and noise signals, we examined 1201 genes from this published dataset with a

182   fold change greater than 1.50 or smaller than 0.667 for down-regulated genes (p<0.05, monocyte

183   compared to naïve microglia), and found that 1066 genes were expressed in our samples

184   (**Supplementary Table 2**). Strikingly, the hierarchical clustering of 525 monocyte- and 541

185   microglia-signature genes revealed that the expression profile of monocyte-derived BEMs (WBRT

186   + CSF-1Ri) does not cluster with naïve (Sham + Control diet), irradiated (WBRT + Control diet)

187   or repopulated (Sham + CSF-1Ri) microglia (**Figure 2d**). Similarity matrix analysis using this

188   microglia/monocyte signature gene list revealed that the expression pattern in BEMs is different

189   from naïve, irradiated and repopulated microglia (**Figure 2e**). Next, we counted genes in each

190   group that expressed in the same trends as microglia or monocyte signature genes from the Lavin

191   data set to determine the similarity scores to these two cell populations. We found that naïve,

192   irradiated and repopulated microglia had 60%, 57% and 51% (718, 685 and 612) genes

193   expressed in the same trends as microglia signature genes, respectively, with minimum similarity

194   (2-3%) to monocyte signature genes; while BEMs expressed both microglia (28%, 331 genes)

195   and monocyte signature genes (32%, 386 genes) (**Figure 2f**). These results further confirm that

196   after microglia depletion and WBRT BEMs originate from blood monocytes.

197

198   *qPCR validation of microglia- and monocyte-specific genes*

199   To validate microglia and monocyte signature genes that were differentially expressed in our

200   RNAseq results we next performed qPCR analyses (**Supplementary Figure 2 and**

201   **Supplementary Table 2**). Microglia signature genes *Sall1*, *P2ry12*, *Tmem119* and *Trem2* were

202   expressed at comparable levels in naïve, irradiated and repopulated microglia, while at

203   significantly lower level in BEMs (**Supplementary Figure 2 a – d**). On the other hand, expression

204   of monocyte signature gene *Runx3*, was significantly higher in BEMs than other groups

205   (**Supplementary Figure 2 e**). Notably, previously reported brain-engrafted macrophage specific

206   genes *Lpar6* and *Pmepa1* [33] have significantly higher expression levels in BEMs after CSF-1Ri

207   and WBRT treatments compared to other groups (**Supplementary Figure 2 f and g**). In addition,

208   the expression of *Ccr2*, a monocyte signature gene that was not differentially expressed in our

209   RNAseq dataset, was also not differentially expressed among the four experimental groups by

210   qPCR (**Supplementary Figure 2 h**). Taken together, these qPCR results validate our RNAseq

211   results and cement the notion that BEMs after microglia depletion and WBRT originate from

212   peripheral monocytes.

213

214   *Monocyte-derived brain-engrafted macrophages resemble embryonic microglia signatures*

215   Because monocyte-derived BEMs were exposed to the brain microenvironment for a short period

216   of time, we hypothesized that they were functionally immature. To test this hypothesis, we first

217   examined genes that were highly expressed at different developmental stages in microglia, and

218   used yolk sac/embryonic and adult-specific genes as references (called embryonic and adult

219   signature genes hereon) [34]. Hierarchical clustering of 1617 embryonic and 785 adult microglia

220   signature genes revealed that transcriptomes of BEMs were highly similar to embryonic microglia,

221   while the transcriptomes of microglia from other groups were similar to adult microglia and did not

222   resemble the embryonic one (**Supplementary Figure S3a**). In addition, a similarity matrix

223   analysis using all 2402 overlapped genes between two datasets showed that BEMs had the

224   lowest similarity with microglia from other groups (**Supplementary Figure S3b**). In addition, 54%

225   of the listed genes (n=1306) in BEMs expressed in the same trends as *yolk sac*/embryonic

226   microglia compared to adult microglia (**Supplementary Figure S3c**). In contrast, naïve (Sham),

227   irradiated (WBRT only) and repopulated microglia (CSF-1Ri only) had much lower embryonic

228   signature similarity scores (16%, 19% and 17%, n=381, 445 and 405, respectively,

229   Supplementary Figure S3c). Notably, naïve, irradiated and repopulated microglia transcriptomes

230   had high adult signature similarity scores (69%, 59% and 63%, n=1649, 1409 and 1507,

231   respectively), while BEMs had the lowest adult similarity score (32%, n=759). These data suggest

232   that the monocyte-derived BEMs start to resemble microglia by expressing more embryonic than

233   adult microglia transcriptomic signature genes.

234

235   *Radiation-induced aberrant phagocytosis activity is abrogated in brain-engrafted macrophages*

236   Aberrant loss of synapses during neuroinflammatory conditions has been linked with increased

237   engulfment of synaptic compartments by microglia [35]. To determine if WBRT affects the

238   phagocytosis potency of microglia, we injected pre-labeled synaptosomes from a naïve donor

239   mouse into the hippocampi of mice after WBRT and CSF-1R inhibitor treatment and measured

240   engulfment by microglia using flow cytometry (**Figure 3a**). After WBRT there was a significant

241   increase in the number of microglia engulfing synaptosomes in the hippocampus compared to

242   naïve non-irradiated animals (**Figure 3b**). Strikingly, synapse engulfment activity was unchanged

243   compared to naïve animals in animals treated with CSF-1R inhibitor during WBRT (**Figure 3b**).

244   Immunofluorescent imaging at the injection sites confirmed that the injected synaptosomes were

245   indeed engulfed by microglia, and the increased trend of engulfment by irradiated microglia

246   remained unchanged (**Figures 3 c and d, Supplementary Figure 4a).** Notably, after

247   hippocampal injection of fluorescent labeled latex beads into the hippocampus, we found that

248   WBRT resulted in increased engulfment of latex beads was also inhibited by CSF-1R inhibitor

249   treatment, suggesting that the WBRT-induced increase of engulfment was not specific to

250   synaptosomes, but rather a general increase of phagocytosis potency (**Supplementary Figure

251   4b**). These data are the first to demonstrate that WBRT results in an increase in microglial

252   phagocytosis activity in the hippocampus that can be prevented by transient microglia depletion

253   and full repopulation.

254

255 *Irradiation-induced complement and phagocytic receptors expression in microglia are absent in*

256 *BEM after WBRT.*

257 Microglial complement receptors play essential roles in physiologic synaptic elimination during

258 development and aberrant elimination during neuroinflammatory conditions [35, 36]. To understand

259 the mechanisms of increased microglia phagocytic activity after WBRT, we measured expression

260 levels of a list of complement receptors, phagocytic markers and lysosome proteins in microglia

261 by flow cytometry. The expression of complement receptor C5aR was significantly elevated in

262 microglia at one month after WBRT. However, in animals treated with CSF-1Ri C5aR expression

263 was unchanged from naïve animals (**Figure 3e**). The same trend was observed in the expression

264 levels of CD68 and lysosomal-associated membrane protein 1 (LAMP-1) (**Figure 3 f and g**).

265 These results were consistent with our data demonstrating decreased PSD95 levels (Figure 3b)

266 and increased microglial phagocytosis activity in the hippocampus after WBRT (**Figure 3 b and**

267 **d**). In addition, complement receptor CR3 (CD11b) was significantly elevated in microglia after

268 WBRT or CSF-1Ri treatments alone, and remained unchanged in BEMs with combined WBRT

269 and CSF-1Ri treatments (**Supplementary Figure S5a**). No changes in the complement receptor

270 C3ar1 were measured after WBRT or CSF-1R inhibitor treatment (**Supplementary Figure S5b**).

271 These results demonstrate that the increased microglia phagocytosis of synaptosomes after

272 WBRT was associated with increased phagocytic and lysosome proteins, and was likely through

273 the complement pathways.

274

275 *Brain-engrafted macrophages after microglia depletion persist in the brain*

276 To determine whether BEMs are present long-term in the brain, we monitored this cellular

277 population for 6 months after WBRT. To eliminate the limitation of using bone marrow obtained

278 from the Cx3cr1$^{+/GFP}$Ccr2$^{+/RFP}$ knock-in reporter mouse strain, we used an actin-GFP transgenic

279 line as bone marrow donors and generated chimeras using the same body-only irradiation

280 protocol (**Figure 4 a**). Six weeks later, mice were treated with CSF-1R inhibitor and WBRT and

281 then used to trace BEMs at varies time points (**Figure 4 a**). Whole coronal sections at the level of

282 the dorsal hippocampus were stained with Iba1 and imaged to quantify total Iba1+ and GFP+

283 cells (**Supplementary Figure 6 a**). We found that all GFP+ cells in the brain were also Iba1+,

284 suggesting that BEMs were indeed derived from the periphery. In addition, the morphology of

285 Iba1+GFP+ BEMs were analyzed and compared to Iba1+GFP- microglia (**Figure 4 b and d**). We

286 found that round-shaped Iba1+GFP+ BEM cells entered the brain starting from 7 days after WBRT,

287 and started to obtain more processes that resembled microglia morphology (**Figure 4 b**). However,

288 Sholl analysis demonstrated that the morphology of BEMs remained stable from 33 days after

289 WBRT and never reached the structural complexity of microglia (**Figure 4c, Supplementary**

290 **Figure S7**). We found that 40 – 90% of Iba1+ cells are also GFP+ at 14 days after WBRT. This

291 ratio remained at high levels at 1, 3 and 6 months after WBRT (**Figure 4 e**). Interestingly, although

292 the Iba1+ and Iba1+GFP+ cell numbers are not fully recovered at 14 days after WBRT, the

293 microglia replacement ratio was similar to the level of later time points (Figure 5 e and

294 Supplementary Figure S6 b and c), suggesting a non-competitive manner of brain parenchyma

295 occupancy by microglia and BEMs. These data demonstrate that BEMs enter the brain shortly

296 after WBRT, adapt to a microglia-like morphology and maintain a stable population.

297

298 *BEMs provide long-term protection against WBRT-induced memory deficits and hippocampal*

299 *dendritic spine loss*

300 To measure the long-term cognitive outcomes, we treated a batch of wildtype animals, and tested

301 their recognition memory at 3 and 6 months after WBRT (**Figure 5 a**). We found that WBRT

302 resulted in persistent loss of recognition memory also at 3 and 6 months, while CSF-1Ri treatment

303 alone did not alter recognition memory performance (**Figure 5 b and c**). Strikingly, mice that

13

304   received WBRT along with temporary microglia depletion did not show any memory deficits and

305   performed undistinguishable from control animals at 3 and 6 months (**Figure 5 b and c**). Our

306   previous report demonstrated that WBRT-induced dendritic spine loss in hippocampal neurons

307   was fully prevented by temporary microglia depletion during irradiation (**Figure 5 d,** replotted

308   using previously published data) [13]. In this study, we sought to understand if the protective effects

309   persisted up to 6 months after WBRT. Our results clearly show that radiation-induced loss of

310   dendritic spines in hippocampal neurons persists to this time point, and that the protective effect

311   of microglia depletion and subsequent replacement by BEMs is long lasting (**Figure 5 e**). Taken

312   together, brief depletion of microglia during WBRT induces sustainable BEMs in the brain and

313   provides long-term protection against irradiation-induced deficits in recognition memory.

314

315   *Replacement of microglia by BEMs protects against concussive injury-induced memory loss*

316   To investigate the function of BEMs after they replaced microglia, a single mild concussive Closed

317   Head Injury (CHI) was given to mice 30 days after CSF-1R inhibitor treatment and WBRT;

318   microglia/BEMs morphology and phagocytic activities were measured following recognition

319   memory test by NOR (**Fig 6 a**). By FACS analysis at 24 days post injury, we found that

320   phagocytosis activity increased (p=0.0419) after CHI in microglia but not in BEMs (**Figure 6 b**).

321   Quantification of immunofluorescent staining of Iba-1/PSD-95 co-localization revealed a trend of

322   increased engulfment towards pre-stained synaptosomes by microglia but not by BEMs (**Fig 6 c**

323   **and d**). In addition, the structural complexity of microglia decreased in Sholl analysis, while the

324   morphology of BEMs remained unchanged after CHI (**Figure 6 e**). Furthermore, at 20 days after

325   injury, CHI-induced recognition memory deficits were spared in mice whose microglia were

326   replaced by BEMs (**Figure 6 f**). These results demonstrate that unlike resident microglia which

327   transition to a less ramified morphology and exhibit increased phagocytic activity towards injected

328   synaptosomes, BEMs remain unchanged in both morphology and phagocytic activity in response

329 to CHI. More importantly, our data suggest that replacement of microglia by BEMs can protect

330 against CHI-induced memory loss.

331

332

333 **Discussion**

334 Here we provide evidence for the direct involvement of microglia phagocytic activity

335 towards synaptic compartments as a mechanistic cause for loss of dendritic spines with

336 consequent impairments in memory functions after WBRT. Replacement of microglia with

337 monocyte derived BEMs prevents loss of synapses and consequent memory deficits. Importantly,

338 BEMs replacing microglia are also protective against a second injury to the brain. Together our

339 results unravel novel immediate and long lasting therapeutic benefits of microglia depletion and

340 repopulation during WBRT.

341 Microglia play pivotal roles in reshaping synaptic networks during neonatal brain

342 development [37, 38]. They engulf synaptic elements by active synaptic pruning in an activity- and

343 complement-dependent manner [38]. Microglia-driven aberrant loss of synapses and consequent

344 impairment of cognitive functions have also been reported in animal models of AD [35], infection [39],

345 injury [40, 41], and aging [42]. Using RNA sequencing, we compared the transcriptomes of microglia

346 from irradiated and non-irradiated brains after CSF-1Ri-mediated microglia depletion and

347 repopulation. WBRT induces increased expression of genes that mainly belong to cell cycle

348 regulation, DNA damage repair and stress-induced biological processes (**Figure 1d**). As a result,

349 activated microglia have higher engulfing potential towards both intrinsic and extrinsic synaptic

350 compartments (**Figures 1 g, Figure 3 b - d**). This view is further supported by the increased

351 expression of endosome/lysosome proteins CD68 and CD107a with the complement receptors

352 CR3 and C5ar1 measured in microglia chronically after WBRT (**Figure 3 e – g, and**

353 **Supplementary Figure 5**). Notably, both endosome/lysosome proteins and complement receptor

354   expressions were comparable to naïve microglia (sham + control diet) in BEMs (WBRT + CSF-

355   1Ri) and repopulated microglia (CSF-1Ri only). These results suggest that the loss of

356   hippocampal synapses after WBRT may be dependent on the activation of the alternative

357   complement pathway. Interestingly, although BEMs are morphologically similar to adult microglia,

358   they retain a transcriptomic signature similar to both circulating monocytes and embryonic

359   microglia (**Figure 2 and Supplementary Figure 3**). It is plausible that the BEMs are in a

360   transitional state between peripheral monocytes and CNS microglia at early developmental

361   stages.

362   The decrease in post-synaptic protein PSD95 level in hippocampal synaptosomes is also

363   paralleled with reductions in hippocampal dendritic spines (**Figures 5 d, e and Feng et al**[13]).

364   However, pre-synaptic Synapsin 1 protein levels are not affected by WBRT or microglia depletion,

365   suggesting that WBRT mainly induces loss of post-synaptic compartments. Interestingly, although

366   the phagocytosis potency of repopulated microglia and BEMs are both low (**Figures 3 b and d**),

367   microglia depletion and repopulation alone does not affect dendritic spine density (**Figures 5 d**

368   **and e**). On the other hand, microglia replacement by BEMs results in increased dendritic spine

369   density compared to those with radiation alone, and microglia depletion alone (**Figure 5 d, data**

370   **re-plotted from Feng et al**[13]). Strikingly, the protective effect of microglia depletion during WBRT

371   results in intact memory functions and extends to 3- and 6-months following irradiation (**Figure 5**

372   **b and c**). The dendritic spine density in mice that received WBRT and CSF-1Ri remained higher

373   than those who only received CSF-1Ri (**Figure 5 e**) suggesting that in an non-reactivate state

374   (evidenced by no changes in genes involved in cell cycle and radiation response, in microglial

375   phagocytosis and lysosome proteins, or in phagocytosis activity towards injected synaptosomes

376   and latex beads) of repopulated microglia and BEMs may have intrinsic differences in maintaining

377   the homeostasis of dendritic spines, which appears to diminish over time.

16

378   In the CNS, microglia maintain a stable population by self-renewal in either a random

379   manner or through clonal expansion [3, 43]. CSF-1R inhibitor treatment alone results in acute

380   depletion of up to 99% of CNS resident microglia, with repopulated microglia arising solely from

381   the residual microglia and their progenitor cells that remain after treatment [8, 44]. The repopulated

382   microglia have transcriptional and functional profiles similar to naïve microglia [9]. Peripheral

383   macrophages can engraft into the brain but remain morphologically, transcriptionally and

384   functionally different from CNS resident microglia [45, 46,]. Under specific circumstances, monocytes

385   entering the CNS can become microglia-like cells. This is most clearly demonstrated in

386   experiments where lethal whole-body irradiation was followed by bone marrow transplantation

387   with labeled monocytes ($Ccr2^+Ly6C^{high}$), resulting in accumulation of these cells in the brain [30]. In

388   neonatal mouse brains monocytes can enter the brain parenchyma without head irradiation and

389   become microglia-like cells at a low frequency [47]. In addition, chronic depletion of microglia without

390   irradiation also results in myeloid cells entering the CNS and becoming BEMs [33]. However, the

391   roles of BEMs in cognitive functions are largely unknown. Here we report that concurrent microglia

392   depletion and therapeutic brain irradiation causes peripheral monocytes to enter the brain

393   parenchyma and become microglia-like BEMs. BEMs enter the brain at 14 days after the

394   completion of brain irradiation, or 4 days after the CSF-1Ri withdrawal (**Figure 4 e, and**

395   **Supplementary Figure 6**). Notably, although the ratio of BEMs was high at this time point the

396   total number of Iba1 positive cells is not fully recovered (**Supplementary Figure 6 b**). This ratio

397   remains at high levels in head-irradiated mice throughout the current study (**Figure 5 e**),

398   suggesting that microglia depletion during WBRT results in sustainable replacement of microglia

399   by BEMs. Importantly, this observation correlates with long-term protection against WBRT-

400   induced loss of recognition memory and dendritic spines in hippocampal granule neurons (**Figure**

401   **6 b – e**).

17

402   In the clinic, cancer patients are unlikely to receive a second round of radiotherapy to the

403   brain. Therefore, instead of introducing a second round of WBRT, after they occupied the brain

404   we gave BEM-bearing mice CHI that causes memory deficits[48, 49], and further examined BEMs'

405   response to a single head trauma. Our data show that microglia had increased phagocytic

406   potential to injected synaptosomes after CHI, while phagocytic activity of BEMs did not change

407   and remained at a similar level as naïve microglia (**Figure 6 b and c**). This is further demonstrated

408   by Sholl analysis of BEMs showing no change in morphology after CHI (**Figure 6 e**). Most

409   importantly, CHI-induced memory deficit was prevented in BEM-bearing mice (**Figure 7 f**). These

410   data are the first to demonstrate that BEMs can prevent brain injury-induced cognitive dysfunction.

411   Further lineage tracing, transcriptomic and functional studies with different microglia

412   depletion models will help answer the following questions: 1) whether the delayed engraftment of

413   BEMs after WBRT seen at day 14 is due to the suppression of cell trafficking from the periphery

414   to the CNS or survival of newly engrafted BEMs that depend on the CSF-1R. 2) The mechanism

415   of the long-term maintenance of BEMs after WBRT. Whether it is achieved by continuous

416   engraftment of new BEMs or by colonization of BEMs that are already in the brain parenchyma.

417   In conclusion we report evidence for the mechanism by which microglia depletion and

418   repopulation after WRBT prevents memory loss. Our results demonstrate that replacement of

419   CNS resident microglia by peripheral monocyte-derived BEMs results in a transcriptional and

420   functional reset of immune cells in the brain to an inactive state, which spares the brain from

421   WBRT-induced dendritic spine loss in hippocampal neurons and recognition memory deficits.

422   Most importantly, replacement of microglia by BEMs protects against concussive brain injury-

423   induced cognitive deficits. These results suggest that replacement of depleted microglia pool by

424   peripheral monocyte-derived BEMs represents a potent treatment for irradiation-induced memory

425   deficits.

426

18

427

Materials and Methods

Animals: All experiments were conducted in compliance with protocols approved by the Institutional Animal Care and Use Committee at the University of California, San Francisco (UCSF), following the National Institutes of Health Guidelines for Animal Care. 7 weeks old C57BL/6J male mice were purchased from the Jackson Laboratory and housed at UCSF animal facilities and were provided with food and water ad libitum. All mice were habituated for one week before any treatments or procedures. 8–10 weeks old $Cx3cr1^{GFP/+}Ccr2^{RFP/+}$ mice were breed by crossing the $Cx3cr1^{GFP/GFP}Ccr2^{RFP/RFP}$ line with wildtype C57BL/6J mice, and used as donors for the bone marrow chimeras.

CSF-1Ri treatment: CSF-1Ri (PLX5622 formulated in AIN-76A standard chow at 1200 ppm, Research Diets, Inc) were provided by Plexxikon, Inc (Berkeley, CA). Mice were given free access to either CSF-1Ri chow or control diet (AIN-76A without PLX5622) for 21 days. Approximately 4.8 mg of PLX5622 was ingested by each mouse per day in the treated group (calculation based on 4 g/mouse daily consumption).

Fractionated whole-brain radiotherapy (WBRT): 8 weeks old mice were injected with ketamine (90mg/kg) /Xylazine (10 mg/kg) mix. When fully immobilized mice were placed in irradiator with cesium-137 source at the dose rate of 2.58 Gy/min. The body was shielded with a lead collimator that limited the radiation beam to a width of 1 cm to cover the brain. Three radiation fractions (3.3 Gy) were delivered every other day over 5 days. Sham animals received ketamine/xylazine without irradiation.

Bone marrow chimeras: 8 weeks old C57BL/6J mice were used as bone marrow recipients. 8 weeks old males received two doses of 6 Gy cersium-137 irradiation at the dose rate of 2.58 Gy/min with head protected by lead plates 6 hours apart. Bone marrow cells from 6–10 weeks old donors $Cx3cr1^{+/GFP}Ccr2^{+/RFP}$ or B6-EGFP (The Jackson Laboratory, stock No 003291) were isolated and resuspended in sterile saline at a concentration of 100 million cells/ml. 0.1 ml of bone

19

453 marrow cells were injected into recipients via retro-orbital injection immediately after the second

454 head protected irradiation. Bone marrow chimeras were housed with 1.1 mg/ml neomycin as

455 drinking water for 4 weeks and allowed an additional 2 weeks to recover before any treatments.

456 **Concussive TBI – Closed head injury:** 12 weeks old C57BL/6J mice were randomly assigned

457 to each TBI or sham surgery group. Animals were anesthetized and maintained at 2-2.5%

458 isoflurane during CHI or sham surgery. Animals were secured to a stereotaxic frame with

459 nontraumatic ear bars and the head of the animal was supported with foam. Contusion was

460 induced using a 5-mm tip attached to an electromagnetic impactor (Leica) at the following

461 coordinates: anteroposterior, −1.50 mm and mediolateral, 0 mm with respect to bregma. The

462 contusion was produced with an impact depth of 1 mm from the surface of the skull with a velocity

463 of 5.0 m/s sustained for 300 ms. Animals that had a fractured skull after injury were excluded from

464 the study. Sham animals were secured to a stereotaxic frame with nontraumatic ear bars and

465 received the midline skin incision but no impact. After CHI or sham surgery, the scalp was sutured

466 and the animal was allowed to recover in an incubation chamber set to 37 °C. All animals

467 recovered from the surgical procedures as exhibited by normal behavior and weight maintenance

468 monitored throughout the duration of the experiments.

469 **Synaptosome isolation staining and injection:** Fresh hippocampi from a naïve mouse was

470 homogenized and spun down in 0.32M sucrose solution (dissolved in 50 mM HEPES buffer).

471 Supernatant was centrifuged in 0.65M sucrose solution at 12,000 rpm for 30 minutes at 4°C. The

472 synaptosome containing pellet was resuspended in 1 x ice-cold PBS, diluted to 100 µg/ml, and

473 stained with PSD-95 antibody (Millipore) on ice for 30 minutes followed by a secondary antibody

474 staining (Invitrogen, goat anti-mouse AF488). Stained synaptosomes were washed and diluted

475 20 times in PBS and stored at -80°C. 2 µl of pre-stained synaptosomes were injected into the

476 right hippocampus of each recipient mouse at the coordinate relative to the bregma: AP + 1.6 mm,

477 ML + 1.6 mm and DV -2.0 mm. Mice were euthanized 3 days later. The left hemispheres

20

478 (uninjected) were used for phagocytosis markers staining and the right hemispheres (injected)

479 were used to assess synaptosome phagocytosis levels by flow cytometry or immunofluorescent

480 staining.

481 **Immunofluorescent Staining:** hemi-brains with synaptosome injection were fixed in 4% PFA

482 overnight, cryo-protected in 30% sucrose solution in 1 x PBS and sliced in 20 μm sections. Sliced

483 tissues were stained with Iba1 (Fujifilm Wako Pure Chemical Corporation, 019-19741) followed

484 by a secondary antibody staining (goat anti-rabbit AF568, Invitrogen, A-11011). DAPI was used

485 for nuclear staining. Images close to the injection site (Supplementary Figure 1a) were taken using

486 a Zeiss Imager Z1 microscope under a 20x objective lens. Tissues from bone marrow chimeras

487 were processed and stained as described above. Images were taken using a CSU-W1 Nikon

488 Spinning Disk Confocal microscope under 10x air, 20x air or 100x immerse oil lenses. All images

489 were analyzed using the Fiji/ImageJ software by experimenters blinded to sample information.

490 **Behavior test:** Novel Object Recognition (NOR) task was used to test hippocampal dependent

491 recognition memory at one, three and six months after the last dose of irradiation. All tests took

492 place during the dark cycle in a room with dim red light as previously described [13, 14]. Briefly, mice

493 were habituated in an open arena (30 cm x 30 cm x 30 cm, L x W x H) for 10 minutes on day one

494 and day two. On day three, two identical objects were put into the arena at a distance of 21 cm

495 and mice were allowed to explore for 5 minutes. On day four, one object was replaced by a novel

496 object and mice were allowed to explore for 5 minutes. All trials were recorded by an overhead

497 camera and analyzed using Ethovision software. Data are presented as discrimination Index,

498 calculated using fomular $DI = (T_{Novel} - T_{Familiar})/(T_{Novel} + T_{Familiar})$.

499 **Flow cytometry:** mice were perfused with cold PBS after euthanasia. Brains were immediately

500 removed and dissociated using a Neural Tissue Dissociation kit (P) (Miltenyi Biotec). Brain cells

501 were resuspended in 30% Percoll solution diluted in RPMI medium, and centrifuged at 800 g for

502 30 minutes at 4°C. Cell pellets were washed with FACS buffer (1 x DPBS with 0.5% BSA fraction

21

503   V and 2% FBS), blocked with mouse CD16/32 Fc block (BD Biosciences #553141) and stained

504   with fluorophore conjugated antibodies (CD11b-AF700, CD45-FITC, BD Pharmingen 557690 and

505   553080, C5aR-PE, CD68-PE and CD107a-PE, Miltenyi Biotec 130-106-174, 130-102-923 and

506   130-102-219), washed with FACS buffer and used for sort or analyses of bone marrow chimera

507   efficiency. Data were collected on an Aria III sorter using the FACSDIVA software (BD

508   Biosciences, V8.0.1), and analyzed with Flowjo software (FlowJo, LLC, V10.4.2).

509   **Flow synaptometry**: after isolation (described above) synaptosomes were stained with PSD-95

510   (Abcam ab13552) or Synapsin-1 (Millipore #1543) antibodies on ice for 30 minutes, washed and

511   followed by a secondary antibody staining (Invitrogen, goat anti-mouse AF488, A-11001). Stained

512   synaptosomes were used immediately for analysis of mean fluorescent intensity measurement.

513   Fluorescent latex beads of 1 μm, 2 μm, 3 μm and 6 μm were used as references of particle sizes

514   in the FSC-A vs SSC-A dot plot. Events between 1 μm and 3 μm were used to measure mean

515   fluorescent intensities of isolated synaptosomes under the FITC channel. Data were collected on

516   an Aria III sorter using the FACSDIVA software, and analyzed with Flowjo software. At least

517   100,000 events were collected from each sample for the analyses.

518   **RNA sequencing:** mRNA was isolated from 100,000 to 400,000 sorted microglia or BEMs using

519   the Dynabeads mRNA DIRECT Purification Kit (Invitrogen #61011) following the manufacturer's

520   instructions. RNA sequencing libraries were generated using the Ovation RNA-seq system V2

521   and Ultralow Library Construction System sample prep kits (NuGEN). Libraries were sequenced

522   on the HiSeq 2500 to generate single end 50bp reads according to the manufacturer's instructions.

523   Normalized per-gene read counts were used to compare relative gene expression levels across

524   samples. Only genes with average read counts greater than 10 were included for analyses.

525   Heatmaps were drawn using the online analysis software Morpheus (Broad Institute,

526   https://software.broadinstitute.org/morpheus), followed by hierarchical clustering using the One

527   minus pearson correlation method. Gene Ontology analysis was performed using the Statistical

528 overrepresentation test (GO biological process complete, PANTHER version 14) [50]. Bar graphs

529 to visualize fold enrichment and p values of enriched GO biological pathways were drawn using

530 the GraphPad Prism software (V 7.01, GraphPad Software, Inc). For analysis of

531 monocyte/microglia signature genes, dataset from Lavin and Winter et al was used as reference

532 (GSE63340) [32]. Genes significantly up or down regulated (p<0.05, fold-change > 1.5 or <0.667)

533 in monocytes vs microglia comparisons are defined as monocyte or microglia signature genes,

534 respectively. Heatmaps were drawn as described above, and similarity matrix were drawn using

535 the Morpheus online tool with Pearson correlation. Monocyte/microglia similarity scores were

536 calculated based on the numbers of genes in each treatment group from this study that expressed

537 in the same trend as monocyte/microglia signature genes (genes with fold-change between

538 0.6667 and 1.500 or with p>0.05 were defined as unspecified). For juvenile/embryonic signature

539 analysis, dataset from Matcovitch-Natan and Winter et al was used as reference (GSE79819) [34].

540 Gene listed to be highly expressed in Yolk Sac and embryonic day 10.5–12.5 were defined as

541 embryonic/juvenile microglia signatures, genes highly expressed in adult

542 cortex/hippocampus/spinal cord were defined as adult microglia signatures. Heatmaps, similarity

543 matrix and similarity scores were drawn or calculated as described above.

544 **qPCR:** mRNAs were extracted from sorted microglia using the Dynabeads mRNA DIRECT

545 Purification Kit (Invitrogen #61011), and reverse transcribed into cDNAs using reverse

546 transcription kit (info) . qPCR reactions were set up in duplicate reactions using the PowerUp

547 SYBR Green Master Mix kit (Applied Biosystems #A25777) using an Mx3000P qPCR System

548 (Agilent, Santa Clara, CA) following the manufacturer's instructions. Data were analyzed using

549 the standard curve method. Standard cDNAs were generated with total RNAs from mixed naïve

550 and irradiated mouse brains. qPCR primers sequences are listed in Supplementary Table 4.

551 **Sholl analysis:** Images of GFP+ (BEMs from bone marrow chimeras) or Iba1+ (AF555, all

552 microglia cells, and BEMs from non-bone marrow chimeras) cells were acquired from stained

23

553 frozen sections (20um) using a confocal microscope under 100x objectives (CSU-W1 Spinning

554 Disk/High Speed Widefield, Nikon). Max Z-projections from Z-stack images (0.26um step size)

555 were used for Sholl analysis[51] in Fiji[52] software using the following settings: manually defined cell

556 center at the cell body, the numbers of intersections between cellular processes and circles with

557 incremental radius (2um step size, up to 60um) were recorded, plotted and compared across

558 samples.

559 **Statistical analyses:** Two-way ANOVA was used to determine radiation and CSF-1Ri treatment

560 effects for NOR, qPCR, flowsynaptometry, flow cytometry, immunofluorescent staining counts

561 and dendritic spine count results, with Tukey's post hoc multiple comparisons. One-way ANOVA

562 with Sidak's post hoc multiple comparisons was used to determine effect of developmental stages

563 for dataset published by Matcovitch-Natan and Winter et al. Unpaired t-test was used to determine

564 differentially expressed microglia/monocyte signature genes from dataset published by Lavin and

565 Winter et al. Unpaired t-test was used calculate the p value of the comparison of BEMs

566 contributions between the BMT and BMT + WBRT groups. Exact p values and numbers of animals

567 used in each experiment were listed in each related figure legend. All error bars represent mean

568 ± SEM.

569

570 **Reference**

571 1. Alliot, F., Godin, I. & Pessac, B. Microglia derive from progenitors, originating from the yolk sac,
572   and which proliferate in the brain. *Developmental Brain Research* **117**, 145-152 (1999).
573 2. Ginhoux, F. *et al.* Fate Mapping Analysis Reveals That Adult Microglia Derive from Primitive
574   Macrophages. *Science* **330**, 841 (2010).
575 3. Ajami, B., Bennett, J.L., Krieger, C., Tetzlaff, W. & Rossi, F.M.V. Local self-renewal can sustain
576   CNS microglia maintenance and function throughout adult life. *Nature Neuroscience* **10**, 1538
577   (2007).
578 4. Prinz, M., Priller, J., Sisodia, S.S. & Ransohoff, R.M. Heterogeneity of CNS myeloid cells and their
579   roles in neurodegeneration. *Nat Neurosci* **14**, 1227-1235 (2011).
580 5. Saijo, K. & Glass, C.K. Microglial cell origin and phenotypes in health and disease. *Nat Rev
581   Immunol* **11**, 775-787 (2011).

582   6.   Hong, S., Dissing-Olesen, L. & Stevens, B. New insights on the role of microglia in synaptic
583   pruning in health and disease. *Current opinion in neurobiology* **36**, 128-134 (2015).
584   7.   Hong, S. & Stevens, B. Microglia: Phagocytosing to Clear, Sculpt, and Eliminate. *Developmental*
585   *Cell* **38**, 126-128 (2016).
586   8.   Elmore, M.R. *et al.* Colony-stimulating factor 1 receptor signaling is necessary for microglia
587   viability, unmasking a microglia progenitor cell in the adult brain. *Neuron* **82**, 380-397 (2014).
588   9.   Elmore, M.R., Lee, R.J., West, B.L. & Green, K.N. Characterizing newly repopulated microglia in
589   the adult mouse: impacts on animal behavior, cell morphology, and neuroinflammation. *PLoS*
590   *One* **10**, e0122912 (2015).
591   10.   Dagher, N.N. *et al.* Colony-stimulating factor 1 receptor inhibition prevents microglial plaque
592   association and improves cognition in 3xTg-AD mice. *Journal of neuroinflammation* **12**, 139
593   (2015).
594   11.   Spangenberg, E.E. *et al.* Eliminating microglia in Alzheimer's mice prevents neuronal loss without
595   modulating amyloid-β pathology. *Brain* (2016).
596   12.   Acharya, M.M. *et al.* Elimination of microglia improves cognitive function following cranial
597   irradiation. *Scientific reports* **6**, 31545 (2016).
598   13.   Feng, X. *et al.* Colony-stimulating factor 1 receptor blockade prevents fractionated whole-brain
599   irradiation-induced memory deficits. *Journal of neuroinflammation* **13**, 215 (2016).
600   14.   Feng, X., Liu, S., Chen, D., Rosi, S. & Gupta, N. Rescue of cognitive function following fractionated
601   brain irradiation in a novel preclinical glioma model. *eLife* **7**, e38865 (2018).
602   15.   Krukowski, K. *et al.* Temporary microglia-depletion after cosmic radiation modifies phagocytic
603   activity and prevents cognitive deficits. *Scientific reports* **8**, 7857 (2018).
604   16.   Rapp, S.R. *et al.* Donepezil for Irradiated Brain Tumor Survivors: A Phase III Randomized Placebo-
605   Controlled Clinical Trial. *Journal of Clinical Oncology* **33**, 1653-1659 (2015).
606   17.   Stupp, R. *et al.* Radiotherapy plus Concomitant and Adjuvant Temozolomide for Glioblastoma.
607   *New England Journal of Medicine* **352**, 987-996 (2005).
608   18.   Greene-Schloesser, D. & Robbins, M.E. Radiation-induced cognitive impairment--from bench to
609   bedside. *Neuro Oncol* **14 Suppl 4**, iv37-44 (2012).
610   19.   Shinohara, C., Gobbel, G.T., Lamborn, K.R., Tada, E. & Fike, J.R. Apoptosis in the Subependyma of
611   Young Adult Rats after Single and Fractionated Doses of X-Rays. *Cancer Research* **57**, 2694-2702
612   (1997).
613   20.   Morganti, J.M., Jopson, T.D., Liu, S., Gupta, N. & Rosi, S. Cranial Irradiation Alters the Brain's
614   Microenvironment and Permits CCR2^{+} Macrophage Infiltration. *PLoS ONE* **9**, e93650 (2014).
615   21.   Warrington, J.P. *et al.* Whole Brain Radiation-Induced Vascular Cognitive Impairment:
616   Mechanisms and Implications. *Journal of Vascular Research* **50**, 445-457 (2013).
617   22.   Hua, K., Schindler, M.K., McQuail, J.A., Forbes, M.E. & Riddle, D.R. Regionally distinct responses
618   of microglia and glial progenitor cells to whole brain irradiation in adult and aging rats. *PLoS One*
619   **7**, e52728 (2012).
620   23.   Chiang, C.S., McBride, W.H. & Withers, H.R. Radiation-induced astrocytic and microglial
621   responses in mouse brain. *Radiotherapy and Oncology* **29**, 60-68 (1993).
622   24.   Mizumatsu, S. *et al.* Extreme Sensitivity of Adult Neurogenesis to Low Doses of X-Irradiation.
623   *Cancer Research* **63**, 4021-4027 (2003).
624   25.   Monje, M.L. *et al.* Impaired human hippocampal neurogenesis after treatment for central
625   nervous system malignancies. *Annals of Neurology* **62**, 515-520 (2007).
626   26.   Fein, J.A. *et al.* Co-localization of amyloid beta and tau pathology in Alzheimer's disease
627   synaptosomes. *The American journal of pathology* **172**, 1683-1692 (2008).

628 27. Prieto, G.A. *et al.* Synapse-specific IL-1 receptor subunit reconfiguration augments vulnerability
629   to IL-1β in the aged hippocampus. *Proceedings of the National Academy of Sciences* **112**, E5078
630   (2015).
631 28. Jung, S. *et al.* Analysis of Fractalkine Receptor CX<sub>3</sub>CR1 Function by
632   Targeted Deletion and Green Fluorescent Protein Reporter Gene Insertion. *Molecular and*
633   *cellular biology* **20**, 4106 (2000).
634 29. Saederup, N. *et al.* Selective Chemokine Receptor Usage by Central Nervous System Myeloid
635   Cells in CCR2-Red Fluorescent Protein Knock-In Mice. *PLoS ONE* **5**, e13693 (2010).
636 30. Mildner, A. *et al.* Microglia in the adult brain arise from Ly-6ChiCCR2+ monocytes only under
637   defined host conditions. *Nat Neurosci* **10**, 1544-1553 (2007).
638 31. Priller, J. *et al.* Targeting gene-modified hematopoietic cells to the central nervous system: Use
639   of green fluorescent protein uncovers microglial engraftment. *Nature Medicine* **7**, 1356-1361
640   (2001).
641 32. Lavin, Y. *et al.* Tissue-resident macrophage enhancer landscapes are shaped by the local
642   microenvironment. *Cell* **159**, 1312-1326 (2014).
643 33. Cronk, J.C. *et al.* Peripherally derived macrophages can engraft the brain independent of
644   irradiation and maintain an identity distinct from microglia. *The Journal of experimental*
645   *medicine* **215**, 1627-1647 (2018).
646 34. Matcovitch-Natan, O. *et al.* Microglia development follows a stepwise program to regulate brain
647   homeostasis. *Science* **353**, aad8670 (2016).
648 35. Hong, S. *et al.* Complement and microglia mediate early synapse loss in Alzheimer mouse
649   models. *Science* (2016).
650 36. Stevens, B. *et al.* The classical complement cascade mediates CNS synapse elimination. *Cell* **131**,
651   1164-1178 (2007).
652 37. Vainchtein, I.D. *et al.* Astrocyte-derived interleukin-33 promotes microglial synapse engulfment
653   and neural circuit development. *Science* **359**, 1269 (2018).
654 38. Schafer, Dorothy P. *et al.* Microglia Sculpt Postnatal Neural Circuits in an Activity and
655   Complement-Dependent Manner. *Neuron* **74**, 691-705 (2012).
656 39. Vasek, M.J. *et al.* A complement-microglial axis drives synapse loss during virus-induced memory
657   impairment. *Nature* **534**, 538-543 (2016).
658 40. Norris, G.T. *et al.* Neuronal integrity and complement control synaptic material clearance by
659   microglia after CNS injury. *The Journal of experimental medicine* (2018).
660 41. Krukowski, K. *et al.* Traumatic Brain Injury in Aged Mice Induces Chronic Microglia Activation,
661   Synapse Loss, and Complement-Dependent Memory Deficits. *International Journal of Molecular*
662   *Sciences* **19** (2018).
663 42. Shi, Q. *et al.* Complement C3-Deficient Mice Fail to Display Age-Related Hippocampal Decline.
664   *The Journal of neuroscience : the official journal of the Society for Neuroscience* **35**, 13029-13042
665   (2015).
666 43. Tay, T.L. *et al.* A new fate mapping system reveals context-dependent random or clonal
667   expansion of microglia. *Nature Neuroscience* **20**, 793 (2017).
668 44. Huang, Y. *et al.* Repopulated microglia are solely derived from the proliferation of residual
669   microglia after acute depletion. *Nat Neurosci* **21**, 530-540 (2018).
670 45. Ajami, B., Bennett, J.L., Krieger, C., McNagny, K.M. & Rossi, F.M.V. Infiltrating monocytes trigger
671   EAE progression, but do not contribute to the resident microglia pool. *Nat Neurosci* **14**, 1142-
672   1149 (2011).
673 46. Yamasaki, R. *et al.* Differential roles of microglia and monocytes in the inflamed central nervous
674   system. *The Journal of experimental medicine* **211**, 1533-1549 (2014).

675 47. Chen, H.-R. *et al.* Fate mapping via CCR2-CreER mice reveals monocyte-to-microglia transition in
676   development and neonatal stroke. *Science Advances* **6**, eabb2119 (2020).
677 48. Chou, A. *et al.* Inhibition of the integrated stress response reverses cognitive deficits after
678   traumatic brain injury. *Proceedings of the National Academy of Sciences* **114**, E6420 (2017).
679 49. Krukowski, K. *et al.* Integrated Stress Response Inhibitor Reverses Sex-Dependent Behavioral and
680   Cell-Specific Deficits after Mild Repetitive Head Trauma. *Journal of Neurotrauma* **37**, 1370-1380
681   (2019).
682 50. Mi, H., Muruganujan, A., Ebert, D., Huang, X. & Thomas, P.D. PANTHER version 14: more
683   genomes, a new PANTHER GO-slim and improvements in enrichment analysis tools. *Nucleic*
684   *acids research* **47**, D419-D426 (2019).
685 51. Ferreira, T.A. & Blackman, A.V. Neuronal morphometry directly from bitmap images. **11**, 982-
686   984 (2014).
687 52. Schindelin, J. *et al.* Fiji: an open-source platform for biological-image analysis. *Nature methods* **9**,
688   676-682 (2012).
689 53. Feng, X. *et al.* Loss of CX3CR1 increases accumulation of inflammatory monocytes and promotes
690   gliomagenesis. *Oncotarget; Vol 6, No 17* (2015).

691

692

Acknowledgements

We thank the Nikon Imaging Center at UCSF for assistance with confocal microscope. We thank the Laboratory for Cell Analysis at UCSF for assistance with FACS sort and analysis.

Author contributions

X.F. conceptualized the study, designed and performed the experiments, analyzed the data and wrote the manuscript. E.F. performed experiments, analyzed the data and wrote the manuscript. M.P performed experiments, analyzed the data and revised the manuscript. D.C. assisted in the in vivo phagocytosis assay and data analysis. Z.B. helped with the in vivo phagocytosis assay imaging and data analysis. M.B. assisted in the Sholl analysis of microglia and BEMs. S.G analyzed the long-term dendritic spine counts data. S.L. provided assistance in experiments related to WBRT and BM chimeras. N.G. provided critical inputs to the study and revised the manuscript. S.R. conceptualized and supervised the study and revised the manuscript. All authors approved the final version of the manuscript.

Competing interests

The authors declare no competing interests.

711 **Figures**
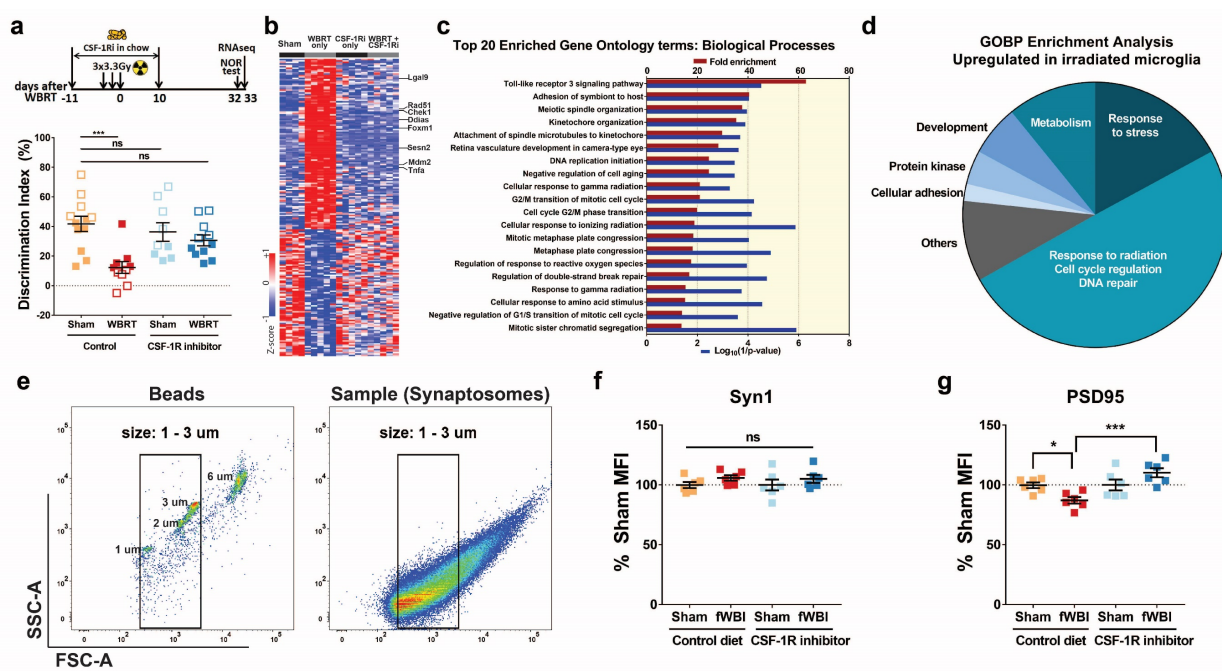
712

713

714 **Figure 1: Microglia depletion and repopulation prevents long term radiation-induced**

715 **memory deficits and loss of hippocampal PSD95. a** experimental design and Novel Object

716 Recognition (NOR) test result. CSF-1R inhibitor was used to deplete microglia during 3 doses of

717 3.3 Gy of whole-brain radiotherapy (WBRT). A 4-day NOR protocol was used to measure

718 recognition memory, which ended on day 32 post WBRT. Microglia were isolated using

719 fluorescent activated cell sorting (FACS) on day 33. and dot plots showing NOR results. Statistical

720 analysis was performed using two-way ANOVA with Dunnett's multiple comparisons test. There

721 is no CSF-1Ri treatment effect ($F_{(1,38)}=1.787$, p=0.1893), but significant WBRT effect ($F_{(1,}$

722 $_{38)}=13.23$, p=0.0008) and interaction between CSF-1Ri treatment and WBRT ($F_{(1,38)}=6.07$,

723 p=0.0184), N = 9-12, animals with insufficient exploration time on NOR test day were excluded.

724 Hollow squares represent animals used in RNA sequencing. **b** hierarchically clustered heatmap

725 showing significantly altered microglial genes by WBRT, but not changed with CSF-1Ri treatment.

726 **c** bar graphs summarizing fold enrichment and p values of the top 20 enriched Biological

727 Processes by Gene Ontology analysis from up-regulated microglial genes after WBRT (full list in

728   Supplementary Table1). No significantly enriched terms were identified by GO analysis from

729   down-regulated genes by WBRT. **d** a pie chart summarizing all enriched GOBP terms. ns= not

730   significant, ***p<0.0001. **e** scatter plots showing gating strategy in flowsynaptometry analyses.

731   Fluorescent beads at various sizes were used as standard to gate isolated hippocampal cell

732   membrane fractions. Particles between 1 μm and 3 μm were considered synaptosomes and used

733   to determine Synapsin1 and PSD95 protein levels by mean fluorescent intensities (MFIs). **f** dot

734   plots to compare Synapsin1 and PSD95 MFI levels in hippocampal cell fractions. Statistical

735   analyses were performed using two-way ANOVA with Tukey's multiple comparisons test. ns = not

736   significant, *p<0.05, ***p<0.001. N=6.
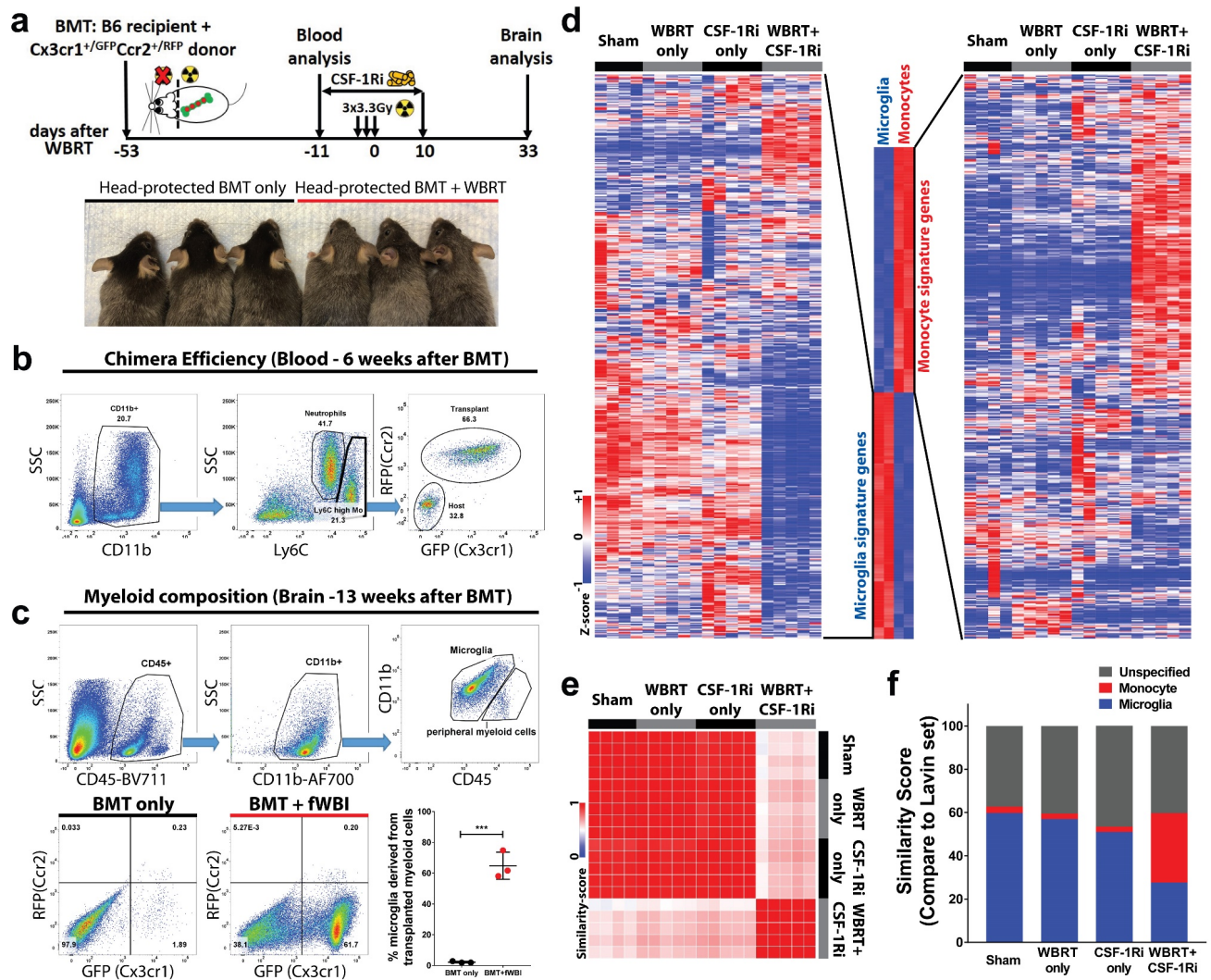
737

738 **Figure 2: Repopulated microglia-like cells after depletion and WBRT originate from**

739 **peripheral monocytes and retain monocytic signatures. a** experimental design of head-

740 protected bone marrow transplantation (BMT) followed by CSF-1Ri-mediated microglia depletion

741 and WBRT. Lower panel shows fur colors before euthanasian for brain analysis. **b** representative

742 FACS analysis gating strategy to analyze bone marrow chimera efficiency 6 weeks after BMT,

743 about two thirds of the CD11b$^+$Ly6C^{high} monocytes are replaced by GFP$^+$RFP$^+$ cells derived from

744 donor bone marrow cells. **c** representative FACS analysis gating strategy and brain myeloid

745 composition results. Upper panel shows FACS gating using CD45 and CD11b staining; microglia

746 and microglia-like cells are defined by positive CD11b staining and low or intermediate CD45

747 levels. Lower panel shows scatter plots of GFP/RFP fluorescent levels of the

748 CD11b$^+$CD45$^{low/intermediate}$ population in the brain, and a dot plot comparing percentages of

749 peripheral myeloid cell derived microglia-like cells. Statistical analysis was performed using

750 unpaired t-test, ***p<0.001. **d** hierarchically clustered heatmaps to compare microglia and

751 monocyte signatures. A signature gene list was defined using a dataset published by Lavin and

752 Winter et al, GSE63340. Defined list and expression details are in Supplementary Table 2). **e**

753 Similarity matrix comparisons using defined monocyte and microglia signature genes. **f** bar graph

754 showing similarity scores to compare relative numbers of genes (in percentage of the defined list)

755 that express in the same trends as monocytes or microglia based on the Lavin and Winter *et al*

756 dataset.

31

757
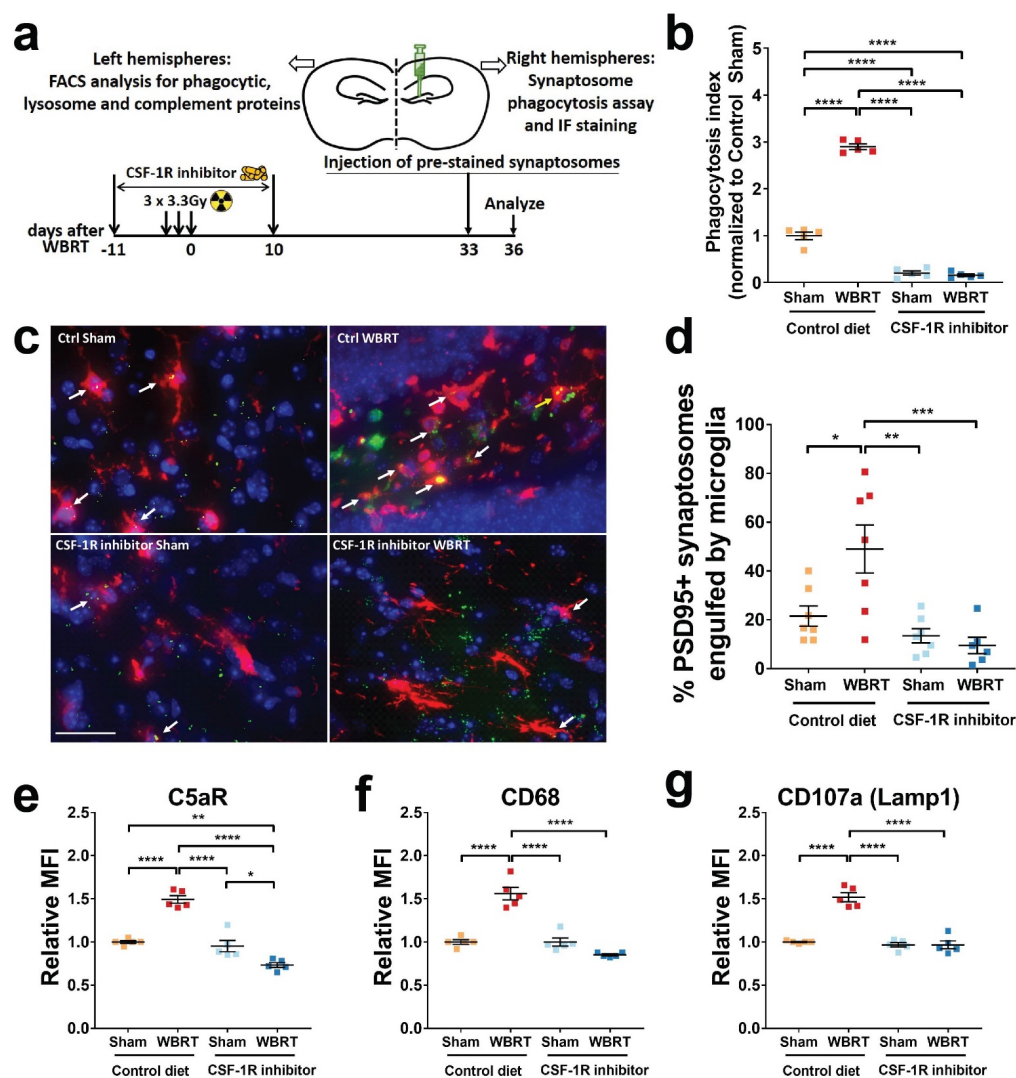
Figure 3: Repopulated microglia and brain-engrafted macrophages are not activated and phagocyte less synaptic compartments. a experimental design for in vivo synaptosome phagocytosis assays. Injection of pre-stained synaptosomes was timed to be the same as previous experiments. Three days later, on day 36 after WBRT, ipsilateral hemispheres were harvested and used for engulfment measurement using FACS or Immunofluorescent staining. **b** FACS analysis result showing levels of microglia that engulfed pre-stained PSD-95 signals. **c** representative images showing engulfment of pre-stained synaptosomes by microglia near injection site. White arrows point at microglia that have engulfed pre-stained synaptosomes. scale bar = 20 μm. **d** dot plot to show quantification result of synaptosome engulfment by

767   immunofluorescent staining. **e − g** dot plots showing cell surface C5aR, and intracellular CD68

768   and CD107a protein levels in microglia and BEMs. Statistical analyses were performed using two-

769   way ANOVA with Tukey's multiple comparisons test. *$p<0.05$, **$p<0.01$, ***$p<0.001$, ****$p<0.0001$.

770   N = 5 − 6.
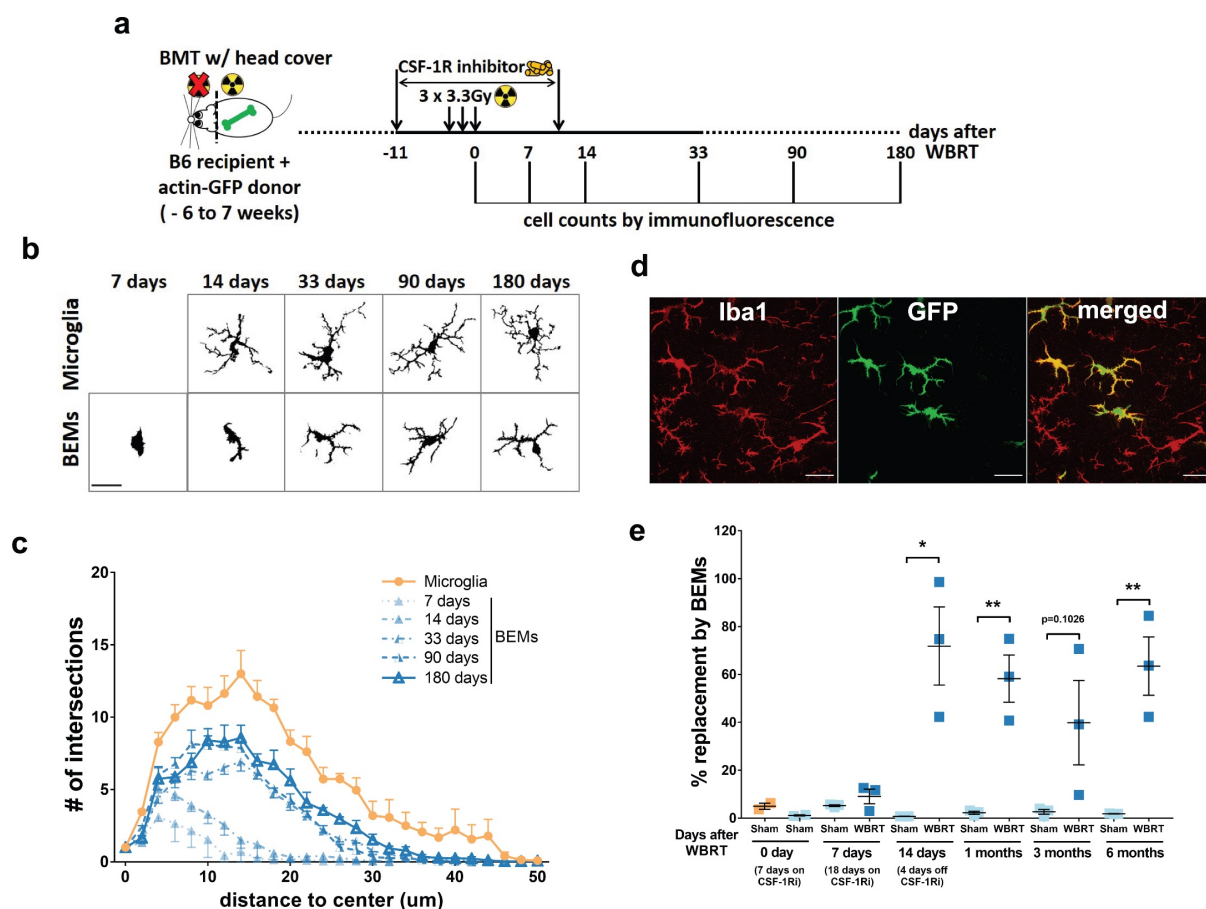
771

772   **Figure 4: BEMs gradually adapt to microglia-like morphology and persist in the brain. a,**

773   schematic of experimental design for long-term assessment of BEMs. **b,** representative images

774   of microglia/BEMs counting, scale bar = 20 μm. **c,** Sholl analysis results showing numbers of

775   intersections at different distances to cell center, BEMs at 7, 14, 33, 90 and 180 days after WBRT

776   were compared to naïve microglia age-matched to 90 days after WBRT., representative images

777   showing differential Iba1 and GFP expressing bprofiles of microglia (Iba1+ GFP-) and BEMs

778   (Iba1+ GFP+) in a BEM bearing brain at 33 days after WBRT. **e**, dot plot to show percentage of

779   replacement of microglia by BEMs, each dot represent an individual mouse. n = 2 - 3. Statistical

780   analyses were performed using unpaired t-test at each distance point (c) or time point (e). See

781   Supplementary Figure 7 for detailed comparisons between microglia and BEMs at each time point.

782
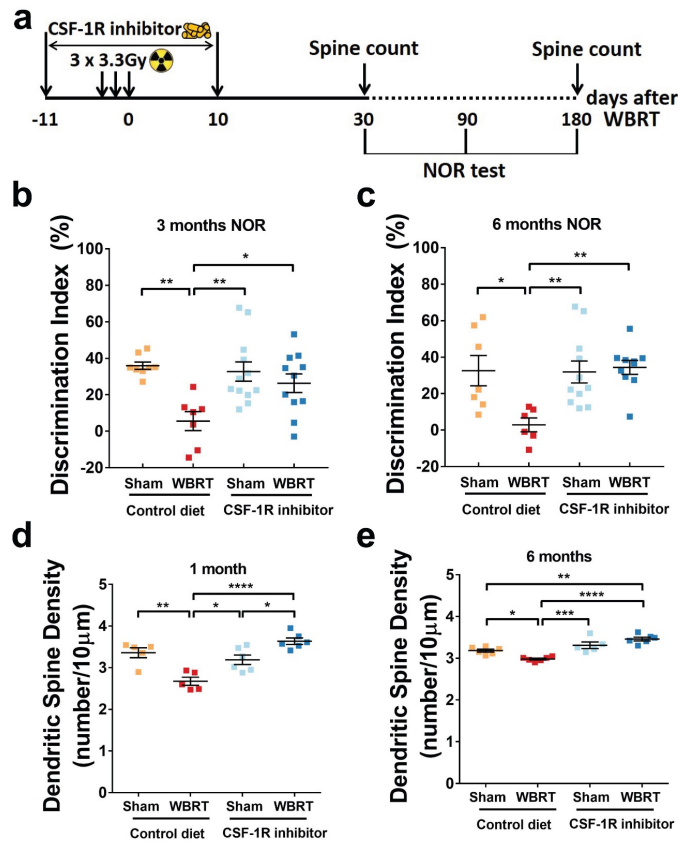
Figure 5: BEMs provide long-term protection against WBRT-induced dendritic spine and memory loss. a schematic of experimental design for long-term memory and dendritic spine density analyses. **b** and **c** dot plots to show NOR test results at 3 and 6 months after WBRT, respectively. N = 6–12. **d** dendritic spine counts of hippocampal granule neurons at 1 month after WBRT (figure reproduced using our previously published data Feng et al[53]). **e** dendritic spine counts of hippocampal granule neurons at 6 months after WBRT, N = 5 – 6.. Statistical analyses were performed using unpaired t-test for each time point (**c**) or two-way ANOVA with Tukey's multiple comparisons test (**e - h**). *p<0.05, **p<0.01, ***p<0.001, ****p<0.0001.

34
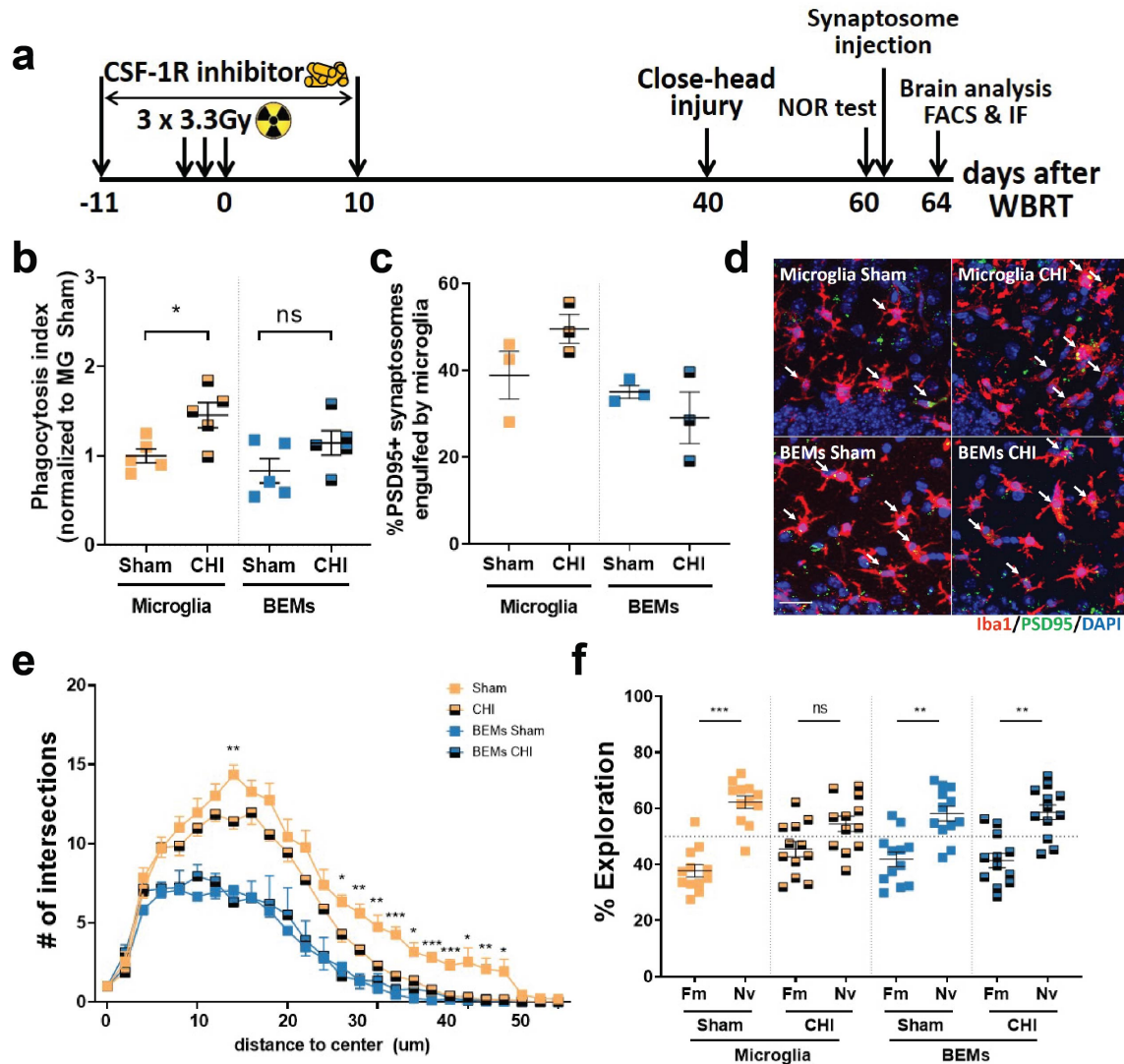
Figure 6: BEMs protects against concussive injury-induced memory deficits. a, schematic of experimental design for concussive injury, cognitive test and following analyses. b, dot plot to show the result of in vivo phagocytosis assay by FACS after injection of pre-stained synaptosomes, each dot represents value from an individual mouse, n = 4 -5. c, dot plot showing result of in vivo phagocytosis assay by IF imaging and quantification, each dot represents mean counts from an individual mouse, n = 3. d, representative images showing microglia and BEMs (arrows) phagocyting injected synaptosomes (green dots). e, Sholl analysis result showing numbers of intersections at different distances to the cell center, n = 5 - 6. f, dot plot showing NOR test result, each dot represent the performance of an individual mouse, n = 12. Statistical analyses

801   were performed using two-way ANOVA with Tukey's multiple comparisons test (b and c) for each

802   distance point (e) or unpaired t-test (f). *$p<0.05$, **$p<0.01$, ***$p<0.001$.

803

804

805